Green Chemistry

PAPER

View Article Online
View Journal | View Issue

Cite this: *Green Chem.*, 2026, **28**, 6442

From semiconductor diversity to mechanistic specificity: S-doped graphitic carbon nitride reprogramming metabolic pathways for bioplastic production

Heng Li, †[a,b] Weidong Zhang,†[b] Ruixiang Zhao,[b] Haiyan Li,[c] Dong Xia*[d] and Yuanpeng Wang *[b]

The integration of photocatalysts with microbial metabolic processes facilitates sustainable solar-driven biosynthesis. However, how photoelectron transfer regulates *Cupriavidus necator* (*C.N*) metabolism under heterotrophic *versus* autotrophic conditions remains unclear, thus restricting the rational design of dual-mode biohybrids for poly-3-hydroxybutyrate (PHB) production. Herein, *C.N* was meticulously coupled with six different semiconductors under illumination, followed by assessment of these constructed biohybrids for heterotrophic and autotrophic PHB production. Among them, S-doped g-C_3N_4 (termed SCN) exhibited the best performance towards heterotrophic PHB production, metabolizing 5.64 ± 0.68 g L^{-1} day^{-1} PHB along with a 208.2% improvement in yield. This enhancement is attributed to the marked biocompatibility and photocatalytic activity of SCN, enabled by its porous structure, narrowed band gap, and improved electrochemical response. Using the same SCN–*C.N* coupling strategy, autotrophic PHB production reached 58.12 ± 0.49 mg L^{-1} day^{-1}, corresponding to a 267.7% increase in productivity. These results establish a dual-mode, metal-free photocatalytic biohybrid platform that operates with an identical catalyst–microbe pairing across both trophic regimes. To elucidate the underlying mechanism, transcriptomic analysis revealed a trophic-state-dependent metabolic reprogramming: heterotrophic PHB production relies primarily on glycolysis and the tricarboxylic acid cycle, whereas autotrophic PHB production is associated with photoelectron transport, oxidative phosphorylation, and CO_2 fixation. Overall, this work clarifies SCN-driven pathway regulation for enhanced PHB biosynthesis and provides a viable green route that integrates high-productivity heterotrophic operation with low-carbon autotrophic operation within a unified abiotic–biotic platform, supporting deeper CO_2-based decarbonization of bioplastic production.

Received 18th January 2026,
Accepted 9th March 2026

DOI: 10.1039/d5gc07072d

rsc.li/greenchem

Green foundation

1. This work advances green chemistry by coupling solar energy and CO_2 with microbial biosynthesis, replacing fossil-derived carbon sources and chemical reductants. It demonstrates a metal-free photocatalyst–microbe system that enables sustainable, light-driven biopolymer production under mild conditions.
2. We achieved significantly enhanced PHB production from CO_2 using solar-driven photoelectrons, while eliminating toxic metals and reducing organic substrate inputs. The work reveals a switch from glycolysis- and TCA cycle-dominated heterotrophic metabolism to photoelectron transport-coupled oxidative phosphorylation and CO_2 fixation under autotrophic conditions.
3. Greenness could be further improved by increasing solar-to-product efficiency, using fully recyclable photocatalysts, integrating waste CO_2 streams, and scaling continuous, low-energy bioprocesses.

[a]*School of Marine Biology, Xiamen Ocean Vocational College, Applied Technology Engineering Center of Fujian Provincial Higher Education for Marine Resource Protection and Ecological Governance, Xiamen Key Laboratory of Intelligent Fishery, Xiamen 361100, China*
[b]*Department of Chemical and Biochemical Engineering, College of Chemistry and Chemical Engineering, Xiamen University, No. 422, Southern Siming Road, Xiamen 361005, China. E-mail: wypp@xmu.edu.cn*
[c]*Tan Kah Kee College, Xiamen University, Zhangzhou, 363105, China*
[d]*State Key Laboratory of Green and Efficient Development of Phosphorus Resources, School of Chemical Engineering and Pharmacy, Wuhan Institute of Technology, Wuhan 430205, China. E-mail: xiadong@wit.edu.cn*
†These authors contributed equally.

1. Introduction

Poly-3-hydroxybutyrate (PHB) is a biodegradable polyester that can be synthesized by a wide range of microorganisms.[1] Due to its excellent biocompatibility, thermoplasticity, and complete biodegradability, PHB has been recognized as one of the most promising alternatives to petroleum-derived plastic.[2] It decomposes naturally into CO_2 and H_2O under environmental conditions, leaving no secondary pollution, and therefore can contribute to reducing plastic waste and carbon emissions.[3,4] Moreover, PHB possesses mechanical and thermal properties comparable to those of polypropylene, making it suitable for packaging, biomedical materials, and agricultural applications.[5]

Conventional PHB production, however, typically depends on heterotrophic fermentation using valuable organic carbon substrates such as sugars, fatty acids, or volatile fatty acids.[4–6] This approach confronts several limitations, including high substrate costs, dependence on agricultural feedstocks, and relatively low carbon-to-product conversion efficiency.[1,7] These drawbacks restrict the large-scale and sustainable production of PHB. Recently, artificial photosynthetic biohybrid systems have emerged as a transformative platform for PHB synthesis.[8–11] By coupling semiconductor photocatalysts with microbial metabolism, these biohybrid systems not only enhance microbial PHB synthesis efficiency under heterotrophic conditions,[8,9] but also enable direct solar-to-chemical energy conversion under autotrophic conditions using light and the inorganic carbon of CO_2 as the sole energy and carbon source.[10,11] This approach mimics natural photosynthesis while concurrently achieving higher energy utilization efficiency and targeted biopolymer synthesis, thus offering a promising route towards sustainable "solar-to-bioplastic" production.

Depending on carbon sources, these biohybrid systems explored for PHB synthesis can be categorized into heterotrophic and autotrophic systems as mentioned above. Specifically, heterotrophic systems typically utilize organic carbon substrates such as glucose or fructose, while autotrophic systems directly employ CO_2 as the sole carbon source, achieving carbon fixation and PHB production *via* photocatalysis or electrocatalysis. As an example, Yu *et al.* constructed a biohybrid system by integrating organic semiconducting polymer dots as photosensitizers with *Ralstonia eutropha* H16 and the electron transport compound neutral red (NR).[11] The photoexcited electrons generated from polymer dots enhanced the intracellular NADPH ratio *via* NR-mediated electron transfer, enabling *Ralstonia eutropha* H16 to convert CO_2 into PHB with a marked yield of 21.3 mg L^{-1}, approximately three times that of the strain alone. In addition, Wang *et al.* developed an inorganic–biological hybrid system composed of the photosynthetic bacterium *Rhodopseudomonas palustris* and CdS nanoparticles (NPs). In this case, under visible-light illumination, the photo-induced electrons from CdS NPs elevated the NADPH cofactor level and promoted the formation of glyceraldehyde-3-phosphate in the Calvin cycle, leading to 148%, 122% and 147% improvements in biomass, carotenoid and PHB yields, respectively.[12] A study reported by Xu *et al.* explored a biohybrid system constructed from g-C_3N_4 and *Cupriavidus necator* (*C.N*), which achieved a PHB yield of 6.73 g L^{-1} using fructose as the substrate.[13] Upon optimization of illumination and aeration conditions, PHB production yield in the g-C_3N_4 and *C.N* constructed biohybrid system further increased up to 12.19 g L^{-1}.[14] It is notable that the same group later established a CdS-NR-*C.N* biohybrid system, with heterotrophic PHB production reaching 1410 mg L^{-1} and autotrophic PHB production reaching 28 mg L^{-1}.[15]

These pioneering studies have demonstrated that coupling semiconductor photocatalysts with microbial metabolism can effectively enhance intracellular reducing power (*i.e.*, generation of NADPH), accelerate the Calvin–Benson–Bassham (CBB) cycle, and promote PHB biosynthesis through improved photoelectron utilization.[11,16] As such, these studies collectively underscore the pivotal role of photo-induced electron transfer in bridging abiotic photocatalysts with intracellular metabolic networks. However, despite these promising advances, several key challenges remain unresolved regarding PHB biosynthesis in photocatalyst–microorganism hybrid systems. However, current studies are constrained by limited semiconductor diversity, the absence of a unified platform that can operate efficiently in both heterotrophic and autotrophic modes, and an incomplete understanding of how photoelectron transfer regulates *C.N* metabolism across these trophic states. Specifically, most existing systems confront limited photocatalyst choice (*e.g.*, either CdS or g-C_3N_4) and often face trade-offs between high photoactivity and poor microbial compatibility. Moreover, the detailed metabolic regulation of *C.N* in heterotrophic and autotrophic biohybrid systems for PHB production lacks a unified understanding. As a result, the fundamental mechanisms of photocatalyst-driven redox reactions coupled with microbial carbon metabolism require further elucidation. This is particularly true for the distinct metabolic pathways governing heterotrophic *versus* autotrophic PHB production. From a green chemistry perspective, many existing photocatalytic biohybrids remain limited by narrow operating modes (either heterotrophic or autotrophic), reliance on heavy-metal photocatalysts, and the lack of a clear pathway for transitioning from high-productivity-targeted operation to CO_2-based biosynthesis. In particular, most reported systems are optimized either for near-term production or for proof-of-concept CO_2 fixation,[10,17,18] with these two factors being rarely considered/practiced within a single, continuous platform, thus resulting in duplicated material development, process redesign, and increased resource demand.

As such, this study establishes a unified, metal-free photocatalytic biohybrid platform that enables both heterotrophic and autotrophic PHB production using the same microbial host (*C.N*) and photocatalytic material (S-doped g-C_3N_4, termed SCN). By systematically comparing six semiconductor photocatalysts (g-C_3N_4, P-doped g-C_3N_4 (PCN), SCN, CdS, Cu-MOF, and Co_3O_4), along with detailed materials characterization, electrochemical analysis, and transcriptomic profiling, this work elucidates how photocatalyst properties and illumination conditions jointly

reprogram microbial metabolism, elucidating that metabolic PHB biosynthesis adopts distinct pathways under heterotrophic and autotrophic modes (Fig. S1). Such mechanism-guided insights provide a rational foundation for future light-energy input reduction and resource efficiency improvement, advancing solar-to-bioplastic biohybrid systems for large-scale green and sustainable high-value compound manufacturing.

2. Materials and methods

2.1. Materials

Graphitic carbon nitride (g-C_3N_4) was synthesized using a conventional thermal polymerization method. Briefly, an appropriate amount of urea was placed in a covered crucible and calcined at 550 °C for 4 h in a muffle furnace. The obtained yellow product was naturally cooled, ground, and collected as g-C_3N_4. Sulfur-doped and phosphorus-doped g-C_3N_4 (denoted as SCN and PCN, respectively) were synthesized as follows: 19 g of urea was thoroughly mixed with 1 g of thioacetamide (for SCN) or 1 g of ammonium dihydrogen phosphate (for PCN), pre-dried at 60 °C for 6 h to remove moisture, and then finely ground to ensure homogeneity. The subsequent calcination, washing, drying, and grinding procedures were identical to those used for g-C_3N_4. The preparation methods for CdS, Cu-MOF, and Co_3O_4 are provided in the SI.

2.2. Microorganism preservation and cultivation

The bacterial strain *C.N* (MCCC 1A07768, originally DSM 428) was obtained from the Third Institute of Oceanography, Ministry of Natural Resources (China). The tryptic soy broth (TSB) medium without glucose contained 17 g L^{-1} tryptone, 3 g L^{-1} soybean peptone, 2.5 g L^{-1} K_2HPO_4, and 5 g L^{-1} NaCl and was sterilized at 121 °C for 20 min. The composition of the nitrogen-limited basal medium is described in the SI.

Stock preservation. *C.N* was first activated in 50 mL TSB at 30 °C and 200 rpm for 12 h (log phase). Then, 750 μL of the culture was mixed with 750 μL of sterile 50% glycerol and stored at −80 °C for long-term preservation.

Heterotrophic cultivation. Activated cells were inoculated at 5% (v/v) into 50 mL of nitrogen-limited medium supplemented with fructose and triethanolamine (TEOA) in 250 mL Erlenmeyer flasks. Cultures were incubated at 30 °C with stirring at 200 rpm. Illumination was provided by LED strips (400 ± 5 nm, 3.07 ± 0.14 mW cm^{-2}).

Autotrophic cultivation. For autotrophic growth, cells were inoculated (5% v/v) into 50 mL of nitrogen-limited medium in 125 mL sealed serum bottles under a mixed gas atmosphere ($H_2 : O_2 : CO_2$ = 7 : 1 : 2). Illumination conditions were identical to those of the heterotrophic system. Detailed cultivation procedures are available in the SI.

2.3. Construction of heterotrophic and autotrophic biohybrid systems

Heterotrophic biohybrid systems for PHB production. The heterotrophic systems were established under the same conditions as those for heterotrophic cultivation. The experimental groups were supplemented with g-C_3N_4, CdS, SCN, PCN, Cu-MOF, or Co_3O_4 under light irradiation, leading to the construction of six biohybrid systems. The naming of experimental groups followed a unified rule, in which each semiconductor–*C.N* biohybrid under illumination was denoted as H-*C.N*@X-light (where X represents the semiconductor material). The denotation of H-*C.N*@SCN-dark is that the experiments were conducted under dark conditions. The control group was maintained without semiconductor addition and without illumination (denoted as H-*C.N*-dark). Cultures were incubated for 120 h, and samples were periodically collected to determine cell dry weight (DCW) and PHB yield.

Autotrophic biohybrid systems for PHB production. Autotrophic biohybrid systems were constructed following the same conditions as those for autotrophic cultivation. The control group was cultured without SCN in the dark (denoted as A-*C.N*-dark), whereas the experimental groups included biohybrid *C.N*@SCN under illumination (denoted as A-*C.N*@SCN-light), *C.N*@SCN in the dark (denoted as A-*C.N*@SCN-dark) and only *C.N* cultured under illumination (denoted as A-*C.N*-light). Cultures were maintained for 72 h, with periodic monitoring of gas consumption, PHB accumulation, and biomass growth.

The heterotrophic and autotrophic experiments were conducted under identical illumination conditions, including the same lamp type (400 ± 5 nm LED strip, 3.07 ± 0.14 mW cm^{-2}), lamp-to-reactor distance (5 cm), irradiation mode (continuous illumination and a 12 h dark/12 h light cycle), and illumination duration (PHB production rate calculated at 48 h). Each of the experiments was performed in triplicate.

2.4. Analytical and characterization methods

Determination of PHB content. PHB quantification was performed by gas chromatography (GC) after methanolysis. An Agilent 7890 GC equipped with an HP-5 column (30 m × 0.32 mm, 5% phenyl-methylpolysiloxane) and a flame ionization detector (FID) was used. Nitrogen, hydrogen, and air were employed as carrier, fuel, and oxidant gases at flow rates of 25, 50, and 350 mL min^{-1}, respectively. The temperature program was as follows: 80 °C (1.5 min) → 140 °C (30 °C min^{-1}, 2 min) → 220 °C (40 °C min^{-1}, 9 min). The injector and detector temperatures were 200 °C and 220 °C, respectively, with a split ratio of 1 : 50 and an injection volume of 1 μL.

Determination of DCW. Pre-dried centrifuge tubes (60 °C, 2 h) were weighed (m_1). Cells were harvested, washed with ultrapure water, freeze-dried for 36 h, and weighed again (m_2).

DCW (g L^{-1}) was calculated using the following equation:

$$\mathrm{DCW} = \frac{m_2 - m_1}{V_1} - c_1$$

where V_1 is the culture volume and c_1 is the semiconductor concentration.

Characterization of semiconductor materials. The morphology of semiconductor samples was analyzed using a Hitachi S-4800 scanning electron microscope (SEM). The specific surface area and pore structure were determined

with a Micromeritics ASAP 2460 analyzer. X-ray diffraction (XRD) patterns were obtained using a Rigaku IV diffractometer (Rigaku, Japan). Fourier-transform infrared (FTIR) spectra were recorded with a Nicolet 6700 spectrometer. Electrochemical impedance spectroscopy (EIS) measurements were performed using an electrochemical workstation (VersaSTAT4-400, AMETEK). UV-Vis diffuse reflectance spectra were recorded on a Shimadzu UV-2600 spectrophotometer equipped with an integrating sphere over the wavelength range of 220–1400 nm.

Characterization of semiconductor–microbe biohybrids. After 24 h of cultivation, 1 mL of microbial suspension was centrifuged at 5000 rpm for 5 min, washed 2–3 times with 0.85% NaCl solution, and resuspended. The cell pellets were stained with a Live/Dead BacLight Bacterial Viability Kit containing SYTO 9 (green fluorescence, live cells) and PI (red fluorescence, dead cells) at a 1 : 1 ratio and incubated in the dark for 20 min. After washing, 10 μL of the stained suspension was placed on a glass slide, covered with a coverslip, sealed, and observed under a confocal laser scanning microscope (CLSM). Excitation/emission settings were 488 nm/500–540 nm for SYTO 9 and 488 nm/600–650 nm for PI.

Cyclic voltammetry measurements. Cyclic voltammetry (CV) experiments were conducted in a single-chamber three-electrode electrochemical cell, using a 150 mL borosilicate glass bottle as the reaction vessel. A graphite plate (20 mm × 20 mm × 1 mm) and an Ag/AgCl electrode (saturated KCl solution) were employed as the counter electrode and the reference electrode, respectively. Preparation of the working electrode: the bacterial cells were inoculated into 50 mL of nitrogen-limited basal medium containing fructose and TEOA, followed by incubation in the dark at 30 °C and 200 rpm for 24 h. Semiconductor materials and sterilized carbon felt (20 mm × 20 mm × 1 mm) were then added to the culture. After 12 h of light cultivation, the carbon felt was removed and used as the working electrode, while the liquid phase served as the culture supernatant. CV curves were recorded using an electrochemical workstation (CSM310, Wuhan KOST Instrument Co., China). The potential window spanned from −1.0 V to 0.6 V (*vs.* Ag/AgCl) at a scan rate of 10 mV s^{-1}.

Transcriptomic analysis. For the heterotrophic biohybrid system, cultures were prepared with light illumination and 0.5 g L^{-1} SCN as the experimental group, while a dark and SCN-free culture served as the control. After 24 h of cultivation (including 1 day of pre-incubation), 1.5 mL of cell suspension was centrifuged, and the pellet was flash-frozen in liquid nitrogen. For the autotrophic biohybrid system, the experimental group was cultured under light with 0.05 g L^{-1} SCN, and the control was maintained in the dark without SCN. Samples (40 mL) were collected at 36 h, centrifuged, and flash-frozen. All samples were sent to Magigene Co., Ltd (Guangdong, China) for transcriptomic sequencing. Total RNA was extracted using the Trizol method, quantified using a Thermo NanoDrop One and an Agilent 4200 TapeStation, and treated with the Epicentre Ribo-Zero™ rRNA Removal Kit. Directional RNA-seq libraries were prepared using the NEBNext® Ultra II™ Directional RNA Library Prep Kit for Illumina and sequenced according to the manufacturer's protocols.

2.5. Data analysis

Graphs and data processing were conducted using OriginPro 8.0, Microsoft Excel, and SPSS. The effects of the coupling materials and illumination were evaluated using *t*-test analysis to determine the significance of differences between the control and experimental groups. A statistical probability of $P < 0.05$ was considered statistically significant.

3. Results and discussion

3.1. Construction of biohybrid systems for heterotrophic PHB production

To construct efficient biohybrid systems for heterotrophic PHB production, different semiconductor photocatalysts were selected, including g-C_3N_4, PCN, SCN, CdS, Cu-MOF, and Co_3O_4. Comprehensions of the physicochemical property discrepancies of such semiconductors help to elucidate their photocatalytic performance differences; therefore, the physicochemical properties of such semiconductor photocatalysts were carefully analyzed and compared. In detail, g-C_3N_4 and CdS possess relatively low band gaps, enabling visible-light response and efficient photoelectron transfer in photocatalysis-coupled microbial reaction systems.[19,20] As the g-C_3N_4 framework is structurally stable and readily modifiable, heteroatom doping with non-metal elements such as P or S can significantly improve its charge separation efficiency and surface reactivity.[21] In contrast, Cu-MOF and Co_3O_4, representing a metal–organic framework and a transition-metal oxide, showcase excellent photocatalytic activity and high charge mobility, which are frequently leveraged to enhance the overall energy conversion efficiency of photofermentation systems.[22,23] With these insights, heterotrophic biohybrid systems were meticulously constructed by integrating *C.N* with each of the semiconductors, leading to the formation of H-*C.N*@g-C_3N_4-light, H-*C.N*@PCN-light, H-*C.N*@SCN-light, H-*C.N*@CdS-light, H-*C.N*@Cu-MOF-light and H-*C.N*@Co_3O_4-light groups for heterotrophic PHB production, where H stands for heterotrophic cultivation and light means experiments were conducted under illumination. The control group H-*C.N*-dark was also built as the blank counterpart and operated under dark conditions.

Experimentally, the *C.N*@CdS-light group exhibited a decrease in heterotrophic PHB production at 48 h, compared with the control group H-*C.N*-dark (Fig. 1a and b), likely due to the cytotoxic effects of CdS that delay cell adaptation. However, the H-*C.N*@g-C_3N_4-light, H-*C.N*@PCN-light and H-*C.N*@SCN-light groups enhanced heterotrophic PHB production significantly, particularly the H-*C.N*@SCN-light group. Detailed analysis indicated that the H-*C.N*@SCN-light group achieved a PHB synthesis rate of 3.12 ± 0.13 g L^{-1} day^{-1}, which was 1.7 times larger than that of the control group H-*C.N*-dark (1.83 ± 0.02 g L^{-1} day^{-1}). In terms of PHB concentration, the H-*C.N*@g-C_3N_4-light and H-*C.N*@PCN-light groups showed

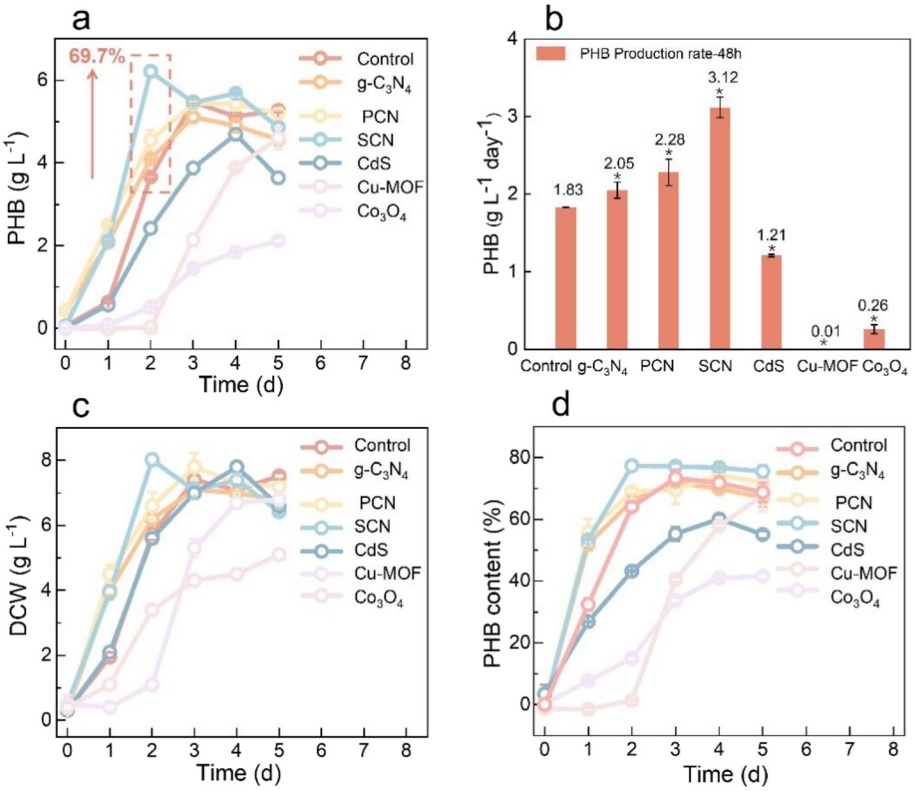

Fig. 1 Constructed biohybrid systems for heterotrophic PHB production, including the experimental groups H-*C.N*@g-C_3N_4-light, H-*C.N*@PCN-light, H-*C.N*@SCN-light, H-*C.N*@CdS-light, H-*C.N*@Cu-MOF-light, and H-*C.N*@Co_3O_4-light and the control group H-*C.N*-dark. (a) Heterotrophic PHB production as a function of reaction period. (b) Heterotrophic PHB production rate at 48 h. (c) DCW accumulation curves over the reaction period. (d) Heterotrophic PHB content (% of DCW) over the reaction period. * indicates a statistically significant difference between the experimental groups and the control group ($p < 0.05$).

moderate improvements, while the H-*C.N*@SCN-light group presented a remarkable improvement from 2.05 to 3.12 g L^{-1} day^{-1}. On top of the marked heterotrophic PHB production, the DCW accumulation rate in the H-*C.N*@SCN-light group was also the highest, reaching 8.02 ± 0.18 g L^{-1} on the second day (Fig. 1c). These results indicate that SCN not only promotes microbial growth but also enhances the intracellular PHB synthesis capacity per biomass unit. Overall, SCN contributes to heterotrophic PHB production substantially, resulting in a 69.7% improvement in total yield compared to the control group H-*C.N*-dark.

Optimization experiments revealed that, when using 40 g L^{-1} fructose and an SCN dosage of 0.5 g L^{-1} under an incubation period of 12 h : 12 h light–dark cycle, the heterotrophic PHB production further reached 5.64 ± 0.68 g L^{-1} day^{-1}, corresponding to a 59.2% improvement relative to the 24 h light group (Fig. S2). It is necessary to point out that continuous illumination inhibited heterotrophic PHB production, with the light-dark cycle (*i.e.*, 12 h of darkness and 12 h of light illumination) exerting a more stable and rapid PHB production performance. This suggests that a continuous illumination period following a dark operation is conducive to heterotrophic PHB production, possibly attributed to the prolonged light exposure causing stress on cell growth while the dark period allowing *C.N* to regulate its metabolism in a manner that is beneficial for heterotrophic PHB production.[24] It is notable that negative contributions to heterotrophic PHB production were observed in the H-*C.N*@Cu-MOF-light and H-*C.N*@Co_3O_4-light groups, particularly in the H-*C.N*@Co_3O_4-light group, in which the accumulation curves of PHB and DCW showed a discernible lag phase. This is likely related to the biotoxicity of Co_3O_4, requiring *C.N* to undergo an adaptation period before resuming its metabolic growth and PHB biosynthesizability.

3.2. Characteristics of the constructed biohybrid interfaces

Following the observed inhibitory effects of Cu-MOF and Co_3O_4 on both microbial growth and heterotrophic PHB production, a comparative investigation was conducted to elucidate the underlying interfacial and electrochemical behaviors of these biohybrid systems. To this end, cyclic voltammetry (CV), an important electrochemical analysis technique, was employed to examine the influence of semiconductors and illumination conditions on the redox behavior, reaction activity, and electrochemical stability of the culture medium. Notably, the CV curve of the culture medium not only exhibited a relatively flat current response over the entire potential range but also displayed a low peak current density (Fig. 2a),

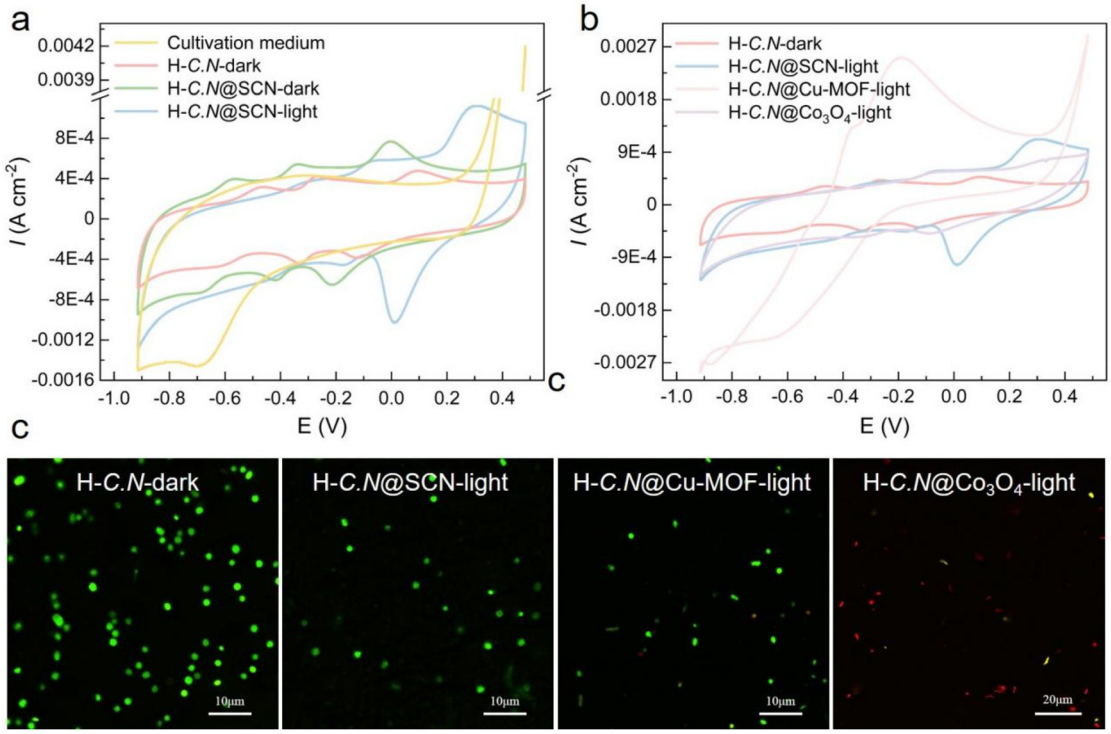

Fig. 2 Electrochemical and biocompatibility characterization of the constructed biohybrid systems. (a) CV curves of the culture medium, the control group H-*C.N*-dark, and the H-*C.N*@SCN-light and H-*C.N*@SCN-dark groups. (b) CV curves of the control group H-*C.N*-dark, and the H-*C.N*@SCN-light, H-*C.N*@Cu-MOF-light and H-*C.N*@Co_3O_4-light groups. (c) Confocal fluorescence images showing live (green) and dead (red) cells, with the H-*C.N*@SCN-light group demonstrating enhanced redox activity and the best microbial compatibility, while the H-*C.N*@Cu-MOF-light and H-*C.N*@Co_3O_4-light groups display evident cytotoxic effects.

suggesting its poor electrochemical activity and the absence of redox-active sites. However, a slight increase in current density was observed only at higher potentials (>0.4 V), confirming that the reactivity of the culture medium is largely constrained by its intrinsic electrochemical properties.[25]

Under light irradiation (Fig. 2a), the current response in the H-*C.N*@SCN-light group increased markedly relative to that of the control group H-*C.N*-dark, implying that SCN enhances electron transfer and redox processes. This current density increase can be attributed to the photo-induced electron–hole pairs generated by the photo-catalytically active SCN, and these photo-induced electron–hole pairs interact with metabolic intermediates or molecules within the microbial medium, thus leading to an overall intensified current signal. Surprisingly, the H-*C.N*@SCN-dark group also displayed a higher current response than the control group H-*C.N*-dark, indicating that SCN is also capable of reacting with metabolites even under dark conditions. This may arise from the residual surface-active sites on SCN, where the doped S species showcase electrochemical reactivity even in the absence of photogenerated charge carriers.[26]

Previous discussion pointed out that the H-*C.N*@Cu-MOF-light and H-*C.N*@Co_3O_4-light groups showed less pronounced enhancement in heterotrophic PHB production. However, a marked difference was found in the CV curve of the H-*C.N*@Cu-MOF-light group, which exhibited the highest current density (Fig. 2b), particularly with a drastic current density rise in the positive potential region, implying its excellent oxidative activity. This may be accredited to the abundant metallic active sites and excellent electrical conductivity of Cu-MOF, collectively facilitating electron transfer rates and redox reactions. In addition to the H-*C.N*@Cu-MOF-light group, the CV curve of the H-*C.N*@Co_3O_4-light group also demonstrated a higher current density than the control group H-*C.N*-dark (Fig. 2b), but it was slightly weaker than that of the H-*C.N*@SCN-light group, possibly attributed to the limited accessible surface-active sites and less favorable band alignment of Co_3O_4. Even though Cu-MOF exhibited superior electrochemical performance, it failed to translate into heterotrophic PHB production enhancement, likely impaired by its biotoxic effects that inactivate microbes.

Biocompatibility is one of the crucial indicators to help understand the observed experimental results; hence, laser scanning confocal microscopy images of H-*C.N*@SCN-light, H-*C.N*@Cu-MOF-light and H-*C.N*@Co_3O_4-light groups were collected, as they exhibited either promotion or inhibition of heterotrophic PHB production. Cell viability is visualized using SYTO 9 and propidium iodide (PI) dual staining, because these dyes differ in their ability to penetrate intact cell membranes, with live cells showing green fluorescence and dead cells emitting red fluorescence. The control group H-*C.N*-dark displayed the densest population of viable cells (Fig. 2c), although some

cell deaths were observed. In the H-*C.N*@SCN-light group, the number of viable cells remained high (Fig. S3), suggesting that the H-*C.N*@SCN-light group has better cell health and higher activity. Notably, the cell mortality in the H-*C.N*@Cu-MOF-light group was greater (Fig. S3), consistent with its cytotoxicity. This helps explain why the H-*C.N*@Cu-MOF-light group with a high electrochemical activity did not exhibit marked performance in heterotrophic PHB production (Fig. 1). Due to the biotoxicity of Co_3O_4, the H-*C.N*@Co_3O_4-light group exhibited intense red fluorescence with only sparse viable cells (Fig. S3). Although bacterial growth continued in the H-*C.N*@Co_3O_4-light group, a large number of dead cells were also found, supporting delayed PHB accumulation (Fig. 1a). Judging by these cell viability analyses, it can be concluded that SCN has the optimal biocompatibility, although a slight inhibitory effect exists. Notably, when collectively considering the material properties and PHB performance metrics of all six semiconductors (Table S1), no clear monotonic relationship is observed between parameters such as specific surface area, pore diameter, or band gap and whether PHB production is promoted or inhibited. Moreover, the electrochemical response (effect on the system current density) also cannot directly predict the PHB outcome across the screened materials. In contrast, the inhibitory effect becomes more pronounced as cytotoxicity increases, suggesting that biocompatibility is a dominant factor shaping the direction and magnitude of the PHB response in these biohybrid systems. As such, semiconductor's biocompatibility and cytotoxicity ought to be considered when designing the biohybrid systems for photosynthesis, as they play crucial roles in determining the overall stability and efficiency of the photosynthetic biohybrid systems.

3.3. Elucidation of the origins of heterotrophic PHB production enhancement

The intrinsic factors conveying the superior photocatalytic activity of SCN need to be studied; hence, the semiconductors g-C_3N_4, PCN, and SCN were carefully characterized. In addition, the photochemical/electrochemical properties of the constructed heterotrophic biohybrid systems were also analyzed. SEM images were collected to examine the morphologies of g-C_3N_4, PCN, and SCN. As observed in Fig. 3a, g-C_3N_4 exhibits sheet-like stacked structures with pronounced aggregation and poor dispersion. As expected, the SEM images of PCN (Fig. 3b) and SCN (Fig. 3c) display similar layered architectures to that of g-C_3N_4. More specifically, PCN shows distinct lamellar stacking with noticeable pores distributed across the sheets, while SCN exhibits a looser yet porous structure with a higher density of pores. It is necessary to emphasize that the presence of copious pores in SCN can provide more active sites for photocatalysis, in turn increasing incident light utilization by improving photon penetration and surface accessibility. The formation of these porous structures stemmed from the release of PH_3 or H_2S gas during the calcination process, tending to create carbon vacancies in PCN and SCN.[27] These produced carbon defects are renowned to suppress the recombination of photogenerated electrons and holes, thereby promoting charge separation and boosting photocatalytic activity.[28]

Nitrogen adsorption measurements were conducted to analyze the specific surface area and pore distribution of g-C_3N_4, PCN and SCN. According to results, g-C_3N_4 exhibited a high specific surface area of 74.8 $m^2\ g^{-1}$, while it reduced to 59.6 $m^2\ g^{-1}$ for PCN and 51.7 $m^2\ g^{-1}$ for SCN. This specific surface area reduction may be attributed to doping-induced morphological and microstructural variations. Notably, all the collected nitrogen adsorption curves displayed type-IV isotherms (Fig. 3d), indicating the formation of mesoporous structures. However, their pore size distributions differed significantly (Fig. 3e). In detail, g-C_3N_4 exhibited a dominant pore diameter of 47.2 nm, which decreased to 21.8 nm in PCN but markedly increased to 67.9 nm in SCN. These results highlight the crucial role of heteroatom doping in regulating pore architectures. Despite the reduced specific surface area in SCN, the concomitant enlargement of pore diameter and enhancement of surface hydrophilicity offset this limitation. Considering the dimensions of *C.N* (approximately 0.4–2.0 μm),[5,29] the pronounced macroporosity (~68 nm, Fig. 3e) of SCN provides geometric advantages for microbial immobilization and mass transfer,[30,31] thus facilitating intimate abiotic–biotic interactions and interfacial electron exchange. As a result, the optimal structural hierarchy of SCN enables to harmonize surface accessibility, pore connectivity, and biocompatibility, jointly contributing to the experimentally observed distinct heterotrophic PHB production.

Optical absorption spectroscopy was conducted to determine the wavelength at which significant light absorption begins, namely, the absorption edge. Assuming that g-C_3N_4, PCN and SCN are direct band-gap semiconductors, their absorption edges were observed at 443.15 nm, 452.86 nm and 695.75 nm (Fig. 3f), corresponding to direct band-gap energies of 2.80 eV, 2.74 eV, and 1.79 eV, respectively (see detailed calculations in the SI). These results verify that SCN can absorb light at longer wavelengths with lower photon energies, thereby extending its visible-light response range and enabling it to utilize a larger fraction of the solar spectrum under identical illumination conditions. The excellent absorption edge feature of SCN facilitates the generation of photogenerated electron–hole pairs and improves the overall light-harvesting efficiency. According to the Tauc plot (Fig. S4), which estimates the optical band gap of semiconductors, the direct band-gap values of g-C_3N_4 and PCN were 2.96 and 2.90 eV, respectively. These values are in close agreement with those estimated from the absorption edges (*e.g.*, 2.80 eV for g-C_3N_4 and 2.74 eV for PCN), supporting the assumption that g-C_3N_4 and PCN are direct band-gap semiconductors. Owing to the direct band-gap characteristics, electrons and holes in g-C_3N_4 and PCN tend to recombine more readily. Notably, the direct band gap of SCN determined from the Tauc plot was 2.21 eV, which deviates substantially from its absorption edge value of 1.79 eV. This distinction implies that SCN is likely an indirect band-gap semiconductor, with the calculated indirect band-

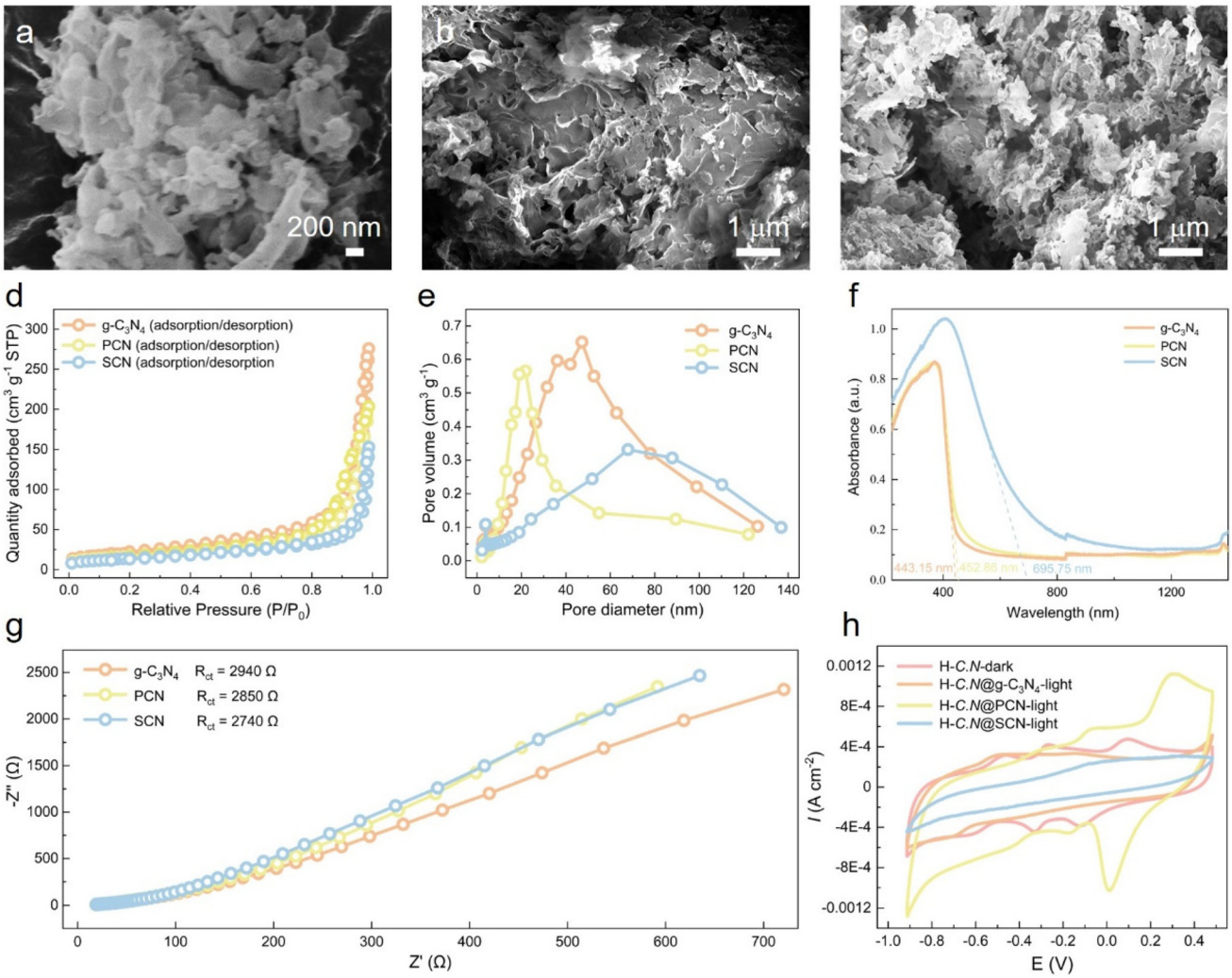

Fig. 3 SEM images of (a) g-C_3N_4, (b) PCN and (c) SCN. (d) Nitrogen adsorption isotherms and (e) pore size distributions of g-C_3N_4, PCN and SCN. (f) UV-Vis diffuse reflectance spectroscopy curves of g-C_3N_4, PCN and SCN. (g) Nyquist plots of g-C_3N_4, PCN and SCN. (h) CV curves of the H-*C.N*@g-C_3N_4-light, H-*C.N*@SCN-light, and H-*C.N*@PCN-light groups.

gap value of around 1.90 eV (Fig. S4). Unlike direct band-gap semiconductors, indirect band-gap semiconductors exhibit slower radiative recombination rates and longer carrier lifetimes, allowing photogenerated electrons to migrate over a larger distance prior to their recombination.[32] These features are conducive to enhancing interfacial charge transfer and photocatalytic stability, making indirect band-gap semiconductors highly suitable for inorganic–biological systems, where sustained electron supply and biocompatibility are of essential importance.

Electrochemical impedance spectroscopy (EIS) was conducted to differentiate the electrochemical properties of g-C_3N_4, PCN and SCN. As shown in Fig. 3g, all curves exhibit a partial semicircle, indicating that charge-transfer processes dominate at high frequencies, while diffusion processes may contribute at lower frequencies. The charge-transfer resistance (R_{ct}) reflects the resistance encountered by electrons moving from the electrolyte to the electrode surface. Analyses pointed out that g-C_3N_4 showcased the largest impedance with an R_{ct} value of 2940 Ω, followed by a slightly reduced R_{ct} value of 2850 Ω for PCN. However, SCN displayed the smallest semicircle diameter and the lowest R_{ct} value of 2740 Ω. EIS results indicated that elemental doping reduces R_{ct} effectively through electrical conductivity and surface activity enhancements. Regarding this point, S-doping formed SCN is particularly effective as it improves interfacial charge transfer, thus accelerating photocatalytic reactions.

Next, we moved forward to characterize the constructed biohybrid systems after heterotrophic PHB production. XRD patterns of the H-*C.N*@g-C_3N_4-light, H-*C.N*@PCN-light, and H-*C.N*@SCN-light groups and the control group H-*C.N*-dark exhibited nearly identical diffraction peaks (Fig. S5a). These peaks are in good agreement with the standard PHB reference pattern from the PDF database (PDF#00-049-2212). This indicates that the crystalline structure of the heterotrophically-produced PHB is consistent with that synthesized from pure *C.N*,

and a small quantity of semiconductors in the constructed biohybrid systems did not interfere with the crystallinity of the produced PHB. In addition, FTIR spectra confirmed that PHB synthesized in all the constructed biohybrid systems possessed the same functional groups (Fig. S5b), again supporting the conclusion that semiconductors have almost no effect on PHB quality. CV curves revealed that the current densities in the H-*C.N*@g-C_3N_4-light and H-*C.N*@PCN-light groups were significantly lower than that in the H-*C.N*@SCN-light group (Fig. 3h), even lower than that of the control group H-*C.N*-dark, implying that the H-*C.N*@g-C_3N_4-light and H-*C.N*@PCN-light groups have weaker electrochemical activity. This can be explained by their intrinsically high electron–hole recombination rates (supported by their direct band-gap characteristic as discussed above), which hamper the participation of photogenerated carriers in redox reactions. Although PCN demonstrates a moderate enhancement in charge separation, its number of active sites and electron mobility remain insufficient to match those of SCN. In short, the direct band-gap features and the large charge-transfer resistances of g-C_3N_4 and PCN cause their less favorable electrochemical behavior. In contrast, S-doping endows SCN with both superior photocatalytic activity and interfacial charge-transfer capability, supporting that the constructed biohybrid system H-*C.N*@SCN-light exhibited the highest heterotrophic PHB production performance.

3.4. Construction of biohybrid systems for autotrophic PHB production

With the successful construction of efficient biohybrid systems for heterotrophic PHB production as described in previous sections, we were then motivated to construct biohybrid systems for autotrophic PHB production, in order to optimize PHB biosynthesizability when using CO_2 as the carbon source instead of consuming high-value substrates in the heterotrophic mode. In light of the high performance of SCN in heterotrophic PHB production, SCN was utilized to construct the autotrophic biohybrid system, which was operated under either light or dark conditions, termed A-*C.N*@SCN-light and A-*C.N*@SCN-dark. The control systems under autotrophic conditions are denoted as A-*C.N*-light and A-*C.N*-dark, where A stands for autotrophic cultivation. According to experimental results (Fig. 4a), the A-*C.N*@SCN-light group presented the highest PHB productivity throughout the entire reaction periods and reached its maximum yield at 48 h, highlighting the synergy enabled by illumination and SCN. In addition, the A-*C.N*@SCN-light group also initiated PHB accumulation earlier, at approximately 36 h (Fig. 4a), suggesting that light exposure enables to advance autotrophic PHB production. In contrast, the A-*C.N*@SCN-dark and A-*C.N*-dark groups exhibited nearly identical PHB production curves, proving that SCN exerts negligible influence on PHB accumulation under dark conditions. Analysis showed that autotrophic PHB production yields followed the trend of A-*C.N*@SCN-light > A-*C.N*@SCN-dark > A-*C.N*-dark > A-*C.N*-light (Fig. 4b). This trend suggests that either illumination (A-*C.N*-light) or SCN incorporation but under dark conditions (A-*C.N*@SCN-dark) might impose certain inhibitory effects, and the inhibitory effects caused by continuous illumination were more pronounced. In addition to PHB production yield, DCW data showed that only the A-*C.N*@SCN-light group exhibited a continuous increase in biomass (Fig. S6).

Importantly, *C.N* in the A-*C.N*@SCN-light group displayed a weaker metabolic activity and lower tolerance to SCN. To reduce such negative effects, the SCN dosage was therefore reduced. These SCN dosage-dependent autotrophic biohybrid systems are abbreviated as A-*C.N*@^{x}SCN-light for simplicity, where x represents the SCN dosage amount. Experimental results demonstrated that the A-*C.N*@$^{0.05}$SCN-light group achieved the highest PHB accumulation of 58.12 ± 0.49 mg L^{-1} day^{-1}, representing a 267.7% improvement relative to the control group A-*C.N*-light, and this value was also higher than those obtained at higher SCN dosages. This dosage-dependent optimum in the autotrophic system likely arises from a balance between photoelectron supply and biological/optical constraints: at 0.05 g L^{-1} SCN, sufficient photoelectron generation/transfer is provided to support CO_2 fixation-driven PHB biosynthesis while maintaining high biocompatibility; in contrast, higher SCN loading can impose greater cytotoxic stress and intensify light scattering/shielding or particle aggregation, thereby reducing effective light utilization and net photoelectron delivery to cells, which ultimately limits autotrophic PHB accumulation. Upon comparison between the A-*C.N*@SCN-light group and the H-*C.N*@SCN-light group, a distinction was that the autotrophic biohybrid group A-*C.N*@SCN-light favored continuous illumination for up to 24 h, while the heterotrophic biohybrid group H-*C.N*@SCN-light performed best under a 12 h : 12 h light–dark cycle (Fig. S7). This distinction may be attributed to *C.N* in the H-*C.N*@SCN-light group relying on external organic carbon sources (*e.g.*, sugars) for its metabolic growth and heterotrophic PHB production, thus weakening its reliance on SCN-induced photocatalysis for energy provision and, consequently, needing only moderate illumination. However, SCN-induced photocatalysis in the A-*C.N*@SCN-light group is of crucial importance to strengthen the metabolism of *C.N*; therefore, continuous illumination is conducive to activating SCN to generate photoelectrons that provide reducing power for *C.N* to drive CO_2 fixation for autotrophic PHB production.

The dynamic consumption of H_2 and CO_2 in the autotrophic biohybrid systems was then analyzed. Specifically, in the A-*C.N*@SCN-light and A-*C.N*@SCN-dark groups, H_2 and CO_2 were consumed rapidly between 24–36 h and 24–48 h, but decreased after 48–60 h. This suggests that illumination helps to enhance the metabolic utilization of H_2 and CO_2 by *C.N*. When 0.1 g L^{-1} SCN was used (A-*C.N*@$^{0.1}$SCN-light), the gas consumption rates became faster, indicating a positive metabolic stimulation by both illumination and SCN. Regarding gas consumption declining after 48 h, this is likely caused by environmental or nutrient limitations within the system, where the microbes approached their stationary phase and the autotrophic PHB production plateaued. In light of these analyses, it is rational that continuous illumination and optimal SCN dosage are

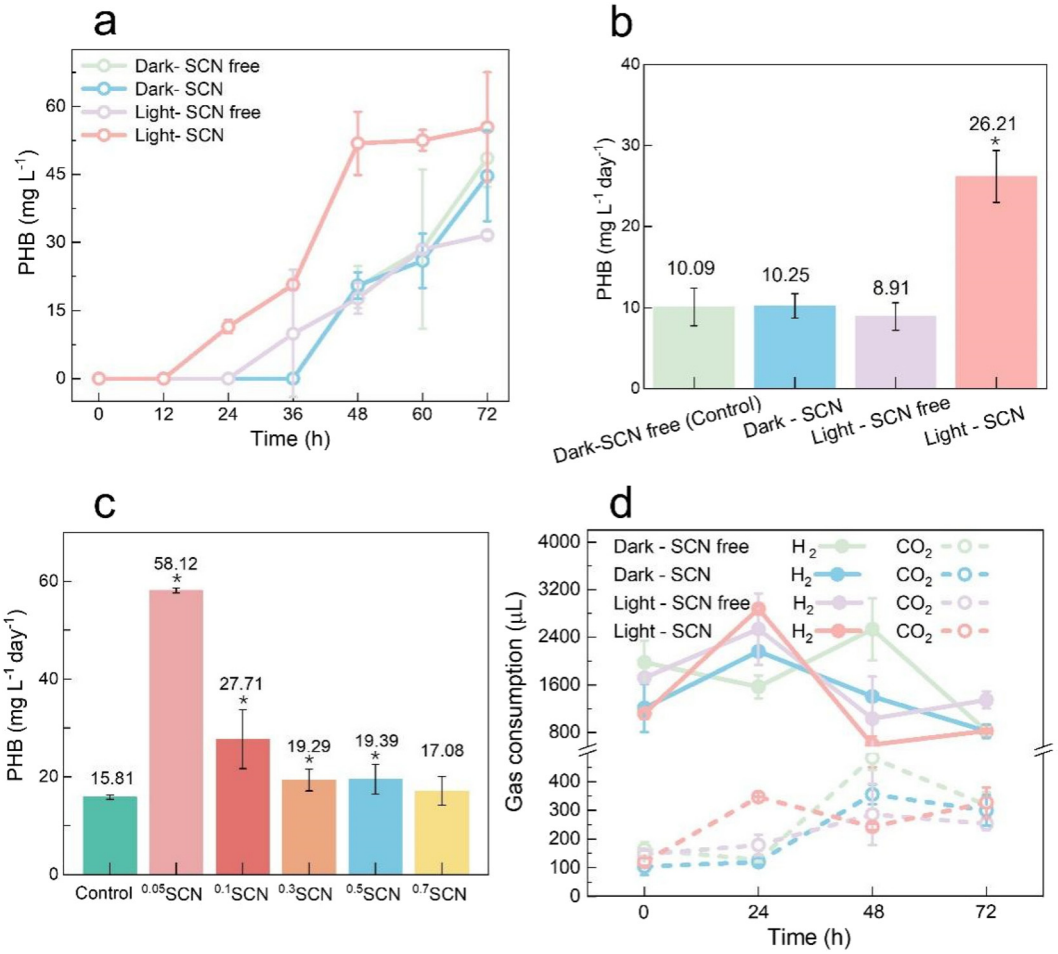

Fig. 4 Performance evaluation of the constructed autotrophic biohybrid systems, including the A-*C.N*@SCN-light and A-*C.N*@SCN-dark groups and the control groups A-*C.N*-light and A-*C.N*-dark. (a) Autotrophic PHB production performance as a function of reaction time. (b) Autotrophic PHB production rate at 48 h. (c) A-*C.N*@^{x}SCN-light with varied SCN concentrations used to affect autotrophic PHB production. (d) Temporal variations regarding CO_2 and H_2 consumption rates. * indicates a statistically significant difference between the experimental groups and the control group ($p < 0.05$).

central to strengthening the autotrophic metabolism of *C.N*, thus ensuring high CO_2 utilization, prolonged system stability and the marked autotrophic PHB synthesizability.

3.5. Transcriptomic analysis to elucidate metabolic regulation in *C.N*

Experimental results not only unraveled the distinct physiological influences on *C.N* in the constructed heterotrophic *versus* autotrophic biohybrid systems, but also confirmed that the A-*C.N*@SCN-light group displayed more promotive effects on microbial metabolism. To elucidate how SCN and light illumination affect gene expression and to uncover the discrepant regulatory mechanisms in these two different biohybrid systems (here specifically focused on the A-*C.N*@SCN-light group and the H-*C.N*@SCN-light group), transcriptomic analysis was therefore performed. According to the correlation heatmap (Fig. 5a), the analyzed samples were clustered into two groups, corresponding to the A-*C.N*@SCN-light group and the H-*C.N*@SCN-light group. The intra-group variability of the A-*C.N*@SCN-light group was higher than that of the H-*C.N*@SCN-light group, and the distance between these two groups was greater, indicating that the autotrophic and heterotrophic biohybrid systems exhibit overall differences in transcriptional expression. The gradual color transition from blue to red reflects the similarity and divergence among samples, providing a solid foundation for subsequent differential gene expression and functional annotation analyses. Expression distribution analysis (Fig. S8) showed that the A-*C.N*@SCN-light group displayed a more elongated shape relative to the H-*C.N*@SCN-light group, inferring a broader distribution, sparser data, and higher variability.

To understand the global expression patterns, principal component analysis (PCA) was applied for dimensionality reduction and visualization. Samples were separated along PC1 and PC2, with PC1 explaining 84.43% of the variance (Fig. 5b), validating the difference between the A-*C.N*@SCN-light group and the H-*C.N*@SCN-light group (namely, the difference between the heterotrophic and autotrophic biohy-

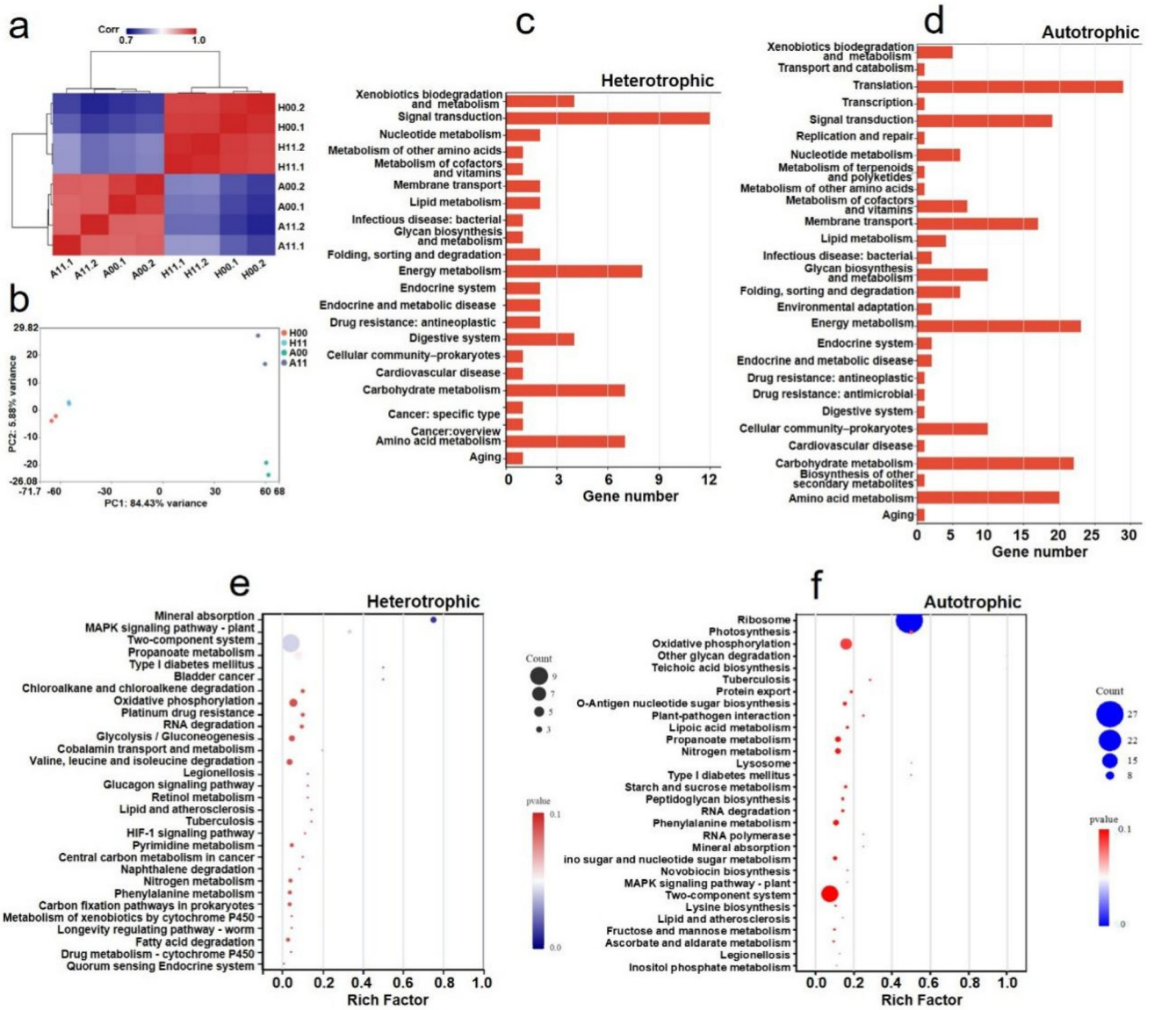

Fig. 5 Comparative metabolomic functional analysis of the heterotrophic biohybrid system H-*C.N*@SCN-light and the autotrophic biohybrid system A-*C.N*@SCN-light. (a) Correlation heatmap showing distinct clustering of the H-*C.N*@SCN-light group and the A-*C.N*@SCN-light group. (b) PCA plot distinguishing metabolic profiles between the H-*C.N*@SCN-light group and A-*C.N*@SCN-light group. KEGG functional annotation of the H-*C.N*@SCN-light group (c) and the A-*C.N*@SCN-light group (d), showing major differences in carbon and energy metabolism. KEGG enrichment analysis illustrating that heterotrophic metabolism proceeded *via* lipid and TCA cycle pathways (e), while autotrophic metabolism is enriched in H_2 metabolism, photosynthetic electron transport, and CO_2 fixation (f).

brid systems). However, PC2 only explained 5.88% of the variance, reflecting the co-influence of light illumination and the SCN photocatalyst. The evident separation of the A-*C.N*@SCN-light group and the H-*C.N*@SCN-light group along PC1 confirms that autotrophic or heterotrophic biohybrid systems lead to significant transcriptional divergence. The insights of PCA results are of crucial importance for subsequent identification of differently expressed genes (DEGs) and the elucidation of metabolic mechanisms.

To identify global shifts in gene groups and metabolic pathways, Kyoto Encyclopedia of Genes and Genomes (KEGG) functional annotation and enrichment analyses were conducted. Results revealed clear differences in metabolic pathway distributions among the heterotrophic biohybrid system H-*C.N*@SCN-light (Fig. 5c) and the autotrophic biohybrid system A-*C.N*@SCN-light (Fig. 5d). In the heterotrophic biohybrid system (H-*C.N*@SCN-light), a greater number of genes were annotated to pathways related to carbon metabolism, amino acid biosynthesis, fatty acid metabolism, and energy production, with more pronounced enrichment found in fatty acid biosynthesis and carbohydrate metabolism. This indicates that, upon feeding the organic carbon of fructose, *C.N* main-

tains a high level of energy generation and reducing equivalents (NADH and ATP), thereby ensuring sufficient carbon skeletons and energy provision for heterotrophic PHB synthesis. Differently, the autotrophic biohybrid system (A-*C.N*@SCN-light) showed greater enrichments in pathways associated with H_2 oxidation, CO_2 fixation, and redox regulation, in which the carbon fixation pathways involve prokaryotes and oxidative phosphorylation. These results suggest that in the absence of external organic carbon or direct consumption of CO_2 for metabolism, *C.N* primarily relies on light-driven electron transfer and SCN-derived reducing power to sustain carbon assimilation and autotrophic PHB production.

KEGG enrichment analysis reveals detailed functional differences. In the heterotrophic biohybrid system (H-*C.N*@SCN-light), enriched pathways included lipid metabolism, pyruvate metabolism, and the TCA cycle, all of which directly participated in the formation of acetyl-CoA (a PHB precursor), reflecting a "carbon-driven, energy-rich and high-throughput synthesis" mode (Fig. 5e). As to the autotrophic biohybrid system (A-*C.N*@SCN-light), significant enrichments were observed in hydrogen metabolism, photosynthetic electron transport, and the Calvin–Benson–Bassham cycle (Fig. 5f). These enrichments in the autotrophic biohybrid system suggest that as the SCN-driven photocatalysis proceeds, photoexcited electrons are transferred through light-induced channels into the intracellular metabolic networks, followed by CO_2 reduction and energy-coupled autotrophic PHB production. Judging from these transcriptomic analyses, it is clear that the heterotrophic biohybrid system H-*C.N*@SCN-light mainly depends on organic carbon oxidation for energy and precursor generation, while the autotrophic biohybrid system A-*C.N*@SCN-light achieves comparable metabolic activation through SCN-assisted photoelectron transfer, highlighting that the metabolism in *C.N* is regulatable in our constructed abiotic–biological biohybrid system for PHB production.

3.6. Elucidation of the distinct metabolic regulation pathways in *C.N*

Based on the understanding of the photosynthetic electron transport chain, the energy conversion mechanisms of the autotrophic and heterotrophic biohybrid systems for PHB production are therefore proposed and illustrated in Fig. 6. Previous studies using CdS nanorods or g-C_3N_4 have achieved the feasibility of semiconductor–microbe hybrid systems for light-driven PHB production.[8,11] However, these reported studies have primarily focused on heterotrophic conditions, consequently lacking systematic pathway validation and investigation into optimized parameters such as illumination. Of novelty, this work introduces a *C.N*@SCN biohybrid platform for photocatalytic PHB production, where we provide a comparative analysis between autotrophic and heterotrophic modes, yielding multi-level mechanistic insights that are corroborated by transcriptomics and KEGG pathway enrichment analysis.

In the autotrophic biohybrid system (A-*C.N*@SCN-light), KEGG pathway analysis revealed significant enrichment in photosynthetic electron transport and oxidative phosphorylation pathways. Specifically, SCN enhances visible-light absorption and charge separation, functioning analogously to an artificial photosystem. Therefore, upon illumination, the photoexcited SCN acts as a PSII-like module by generating high-energy electrons, analogous to water-splitting-derived electrons in oxygenic phototrophs.[33] These electrons are transferred to cellular quinones and iron–sulfur proteins, effectively reinforcing the intracellular reducing pool. Subsequently, the downward electron transfer resembles the function of a PSI-like module, promoting the regeneration of NADPH through ferredoxin-dependent pathways. This semiconductor-enabled pseudo-Z-scheme thus provides both reducing power (NADPH) and enhanced proton-motive force for ATP synthesis, thereby supporting the energetic and reductive demands of the Calvin–Benson–Bassham cycle (Fig. 6a). In addition, SCN generates photoexcited electrons that are efficiently transferred through cytochromes (Cyt), ferredoxin (Fd), and ferredoxin–$NADP^+$ reductase (FNR), forming a continuous chain of photoexcitation → electron transfer → proton translocation → ATP synthesis. These photogenerated electrons convert external photonic energy into NADPH, enabling *C.N* to maintain sufficient reducing power for CO_2 fixation and PHB formation even in the absence of organic substrates. Owing to the efficient photoelectron generation of SCN, continuous 24 h illumination yielded a 267.7% improvement in autotrophic PHB production, verifying that SCN-mediated photoelectron transfer governs autotrophic PHB metabolism.

In the heterotrophic biohybrid system (H-*C.N*@SCN-light), continuous illumination (24 h) increased PHB production by 13.5%, indicating that light exposure indeed provides an auxiliary enhancement to cellular metabolism. Nevertheless, under a 12 h : 12 h light–dark cycle, moderate illumination boosted PHB synthesis by 80.6%, suggesting that appropriate light exposure is more conducive to SCN-mediated photo-assisted electron injection into the cellular respiratory chain, whereas excessive illumination may disrupt redox homeostasis and hinder carbon utilization. Mechanistically, the heterotrophic biohybrid system operates through the oxidative metabolism of organic carbon sources (*e.g.*, fructose and acetate), proceeding from organic carbon oxidation to acetyl-CoA formation and ultimately PHB biosynthesis. In this process, photoexcited electrons are injected into NADH-generating pathways, increasing electron flux and thereby boosting ATP and NADH supply to provide energy and reducing power for PHB synthesis (Fig. 6b). On the other hand, the expression of 3-hydroxyhexanoyl-CoA dehydrogenase is markedly upregulated in the H-*C.N*@SCN-light group (Fig. S9), promoting the conversion of 3-hydroxyhexanoyl-CoA to 3-oxohexanoyl-CoA and thus increasing acetyl-CoA availability, which in turn enhances PHB production. In contrast, the autotrophic biohybrid system A-*C.N*@SCN-light is dominated by light-driven electron transfer, NADPH regeneration, and ATP coupling for CO_2 fixation and PHB production.

Collectively, this study proposes a unified dual-mode model of energy conversion in *C.N*@SCN biohybrid systems, where

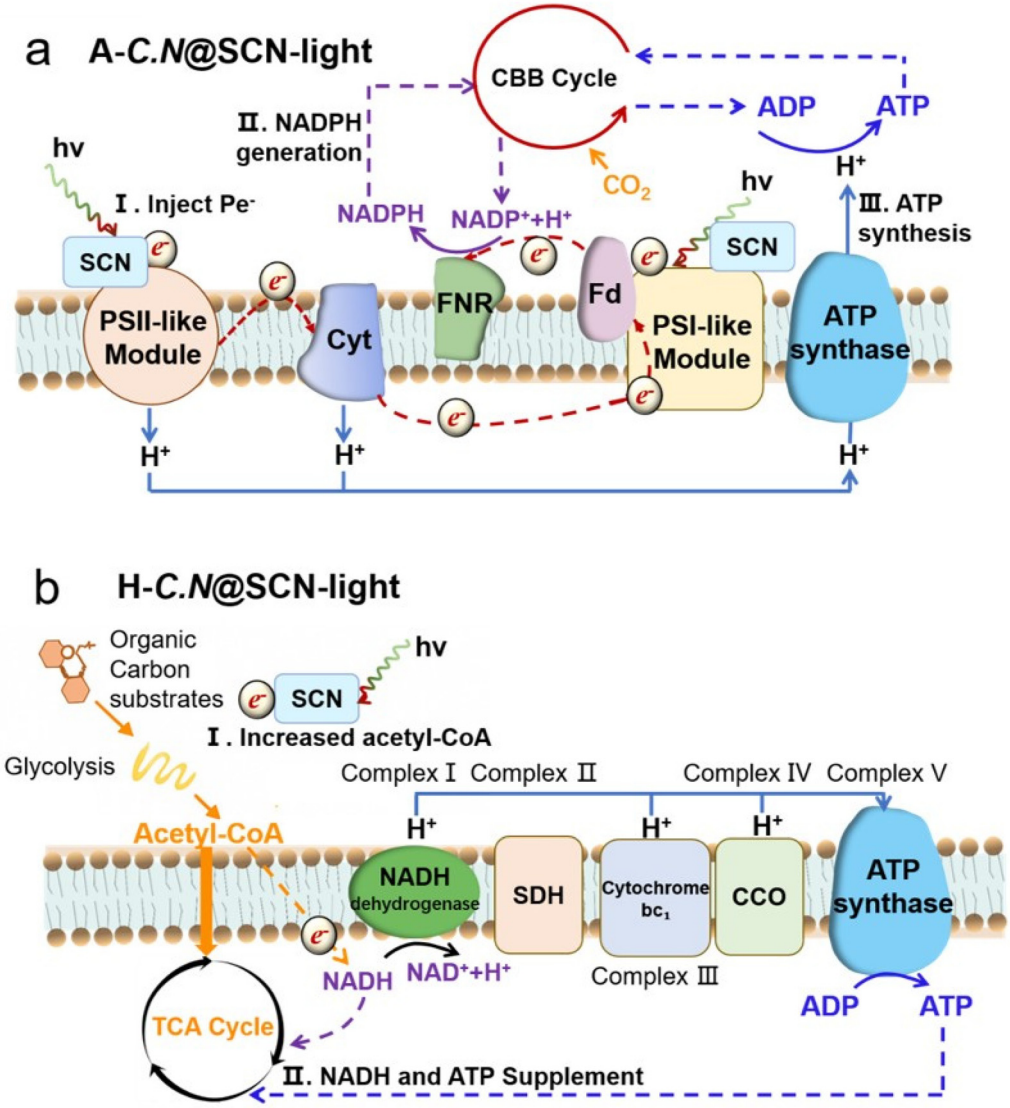

Fig. 6 Schematic illustrations of the proposed energy conversion pathways in the heterotrophic biohybrid system and the autotrophic biohybrid system for PHB production. (a) In the autotrophic biohybrid system A-*C.N*@SCN-light, light-driven electrons transfer through a PSII-like module, a PSI-like module and the cytochrome b_6f complex produces ATP and NADPH for CO_2 fixation. (b) In the heterotrophic biohybrid system H-*C. N*@SCN-light, photoexcited electrons are injected into NADH-generating pathways, increasing electron flux and thereby boosting ATP and NADH production to supply energy and reducing power for PHB biosynthesis, while also increasing acetyl-CoA availability, which in turn enhances heterotrophic PHB production.

autotrophic metabolism for PHB production is governed by semiconductor-mediated photoelectron transfer, while heterotrophic metabolism for PHB production is driven by substrate oxidation with illumination-assisted enhancement. As such, compared to reported CdS or g-C_3N_4, this work delineates the reasons behind why SCN enables remarkable PHB production, uncovers the distinct autotrophic metabolism and heterotrophic metabolisms in *C.N* for PHB production, explains KEGG-based validation of light-driven electron transport and oxidative phosphorylation pathways, and discovers the light-dependent PHB synthesis efficiency. These discoveries together establish a comprehensive mechanistic framework for semiconductor-driven carbon fixation and polymer biosynthesis by using non-photosynthetic bacteria.

3.7. Green advancement analysis of the constructed photocatalytic *C.N*@SCN biohybrid for CO_2-to-PHB conversion

Regarding metabolic CO_2 consumption, our abiotic–biotic system achieves an autotrophic PHB productivity of 58.12 mg L^{-1} d^{-1}, which is comparable to or even higher than recent reported state-of-the-art photocatalytic biohybrids (Table 1). In addition, our abiotic–biotic system also shows a high PHB productivity of 5.64 g L^{-1} d^{-1} in the heterotrophic mode, highlighting its dual-mode operation capability. Crucially, our

Table 1 Summary of photocatalytic biohybrid systems for CO_2-to-PHB production

Components (catalyst–microbe)	Metal-free	Carbon source	Light condition	PHB productivity	Quantum efficiency	Key green feature	Study
S-doped g-C_3N_4 (SCN)–*Cupriavidus necator*	Yes	CO_2 (autotrophic); organic substrate (heterotrophic)	3.07 ± 0.14 mW cm^{-2}	58.12 ± 0.49 mg L^{-1} d^{-1} (autotrophic); 5.64 ± 0.68 g L^{-1} d^{-1} (heterotrophic)	1.27%	Metal-free dual-mode platform; process intensification; specific surface area (m^2 g^{-1})	This study
K/O co-doped g-C_3N_4–*Ralstonia eutropha*	Yes	CO_2	4000 lux (0.75 mW cm^{-2})	49.35 ± 0.85 mg L^{-1} d^{-1}	5.88%	Low-light operation without auxiliary agents	17
Organic semiconductor heterojunctions–*R. eutropha*	Yes	CO_2	Visible light	107.3 mg L^{-1} OD_{600}^{-1}	—	Organic semiconductor–bacteria interface for light harvesting	10
CdS@Au@PDDA–*Cupriavidus necator*	No	CO_2	Visible light	53.6 ± 5.2 mg L^{-1}	—	Plasmon-enhanced activity with Cd-based photocatalyst	18

abiotic–biotic system featuring a dual-mode operation capability enables process intensification and reduces the need for parallel catalyst, strain, and reactor design. Noteworthily, the usage of a metal-free carbon nitride photocatalyst avoids critical or heavy metals, which are commonly observed in CdS-based systems. As such, our abiotic–biotic system not only demonstrates the implementation of green materials for abiotic–biotic systems but also concurrently achieves the goal of realizing remarkable CO_2-to-PHB conversion performance. Consequently, a central green advantage of this study is the establishment of a dual-mode photocatalytic *C.N*@SCN biohybrid platform that operates efficiently under both heterotrophic and autotrophic conditions, when using the identical catalyst–microbe system. In the near term, the heterotrophic mode could enable high-throughput PHB production by consuming renewable organic carbon sources, such as sugars or volatile fatty acids derived from waste streams, thus supporting practical bioplastic synthesis with high space–time yields. In the medium-to-long term, the same platform can be switched to a CO_2-only autotrophic mode, enabling direct carbon fixation and a more deeply decarbonized production route. Importantly, this transition does not require changing either the microbial host (*C.N*) or the photocatalytic material (SCN), more crucially, leading to substantially reduced process reconfiguration, material redundancy, and development expenditure. In addition, the operational continuity of this platform transforms the system from a laboratory demonstration into an implementable green pathway, in which productivity-oriented biosynthesis and low-carbon operation are seamlessly integrated within a unified, metal-free biohybrid framework.

Despite these advantages, the present system does not yet demonstrate superiority in low-light energy demand. Specifically, the autotrophic experiments were conducted at an incident light power density of 3.07 mW cm^{-2}, which is higher than that reported for indoor-light biohybrid systems using low-light energy (*e.g.*, 0.75 mW cm^{-2}).[17] As a result, although the absolute PHB productivity is competitive, the quantum efficiency in this study is 1.27%, which is lower than the reported value of 5.88% in the literature,[17] indicating that further improvements in light utilization efficiency are still required. In particular, optimizing the illumination intensity is expected to enhance photoelectron generation and transfer while avoiding photoinhibition or unnecessary energy input. In addition, the dual-mode operation of our abiotic–biotic system indeed enhances process flexibility; however, the autotrophic productivity is still considerably lower than that achieved under heterotrophic conditions, reflecting inherent limitations in electron utilization and CO_2 assimilation that challenge current photocatalytic biohybrid systems. Hence, future explorations should centralize on optimizing the abiotic–biotic interface (*e.g.*, photocatalyst loading, cell–catalyst contact, and light management within the reactor) along with mechanism-guided metabolic tailoring to improve photoelectron utilization.

For sustainable downstream processing, the intracellular PHB produced in this work can be recovered using greener

routes that reduce halogenated solvents. After biomass harvesting (*e.g.*, centrifugation), PHB may be extracted with non-halogenated, recyclable solvents (*e.g.*, ethyl acetate or dimethyl carbonate) followed by anti-solvent precipitation (*e.g.*, ethanol) and solvent recycling.[34] Alternatively, mild digestion of non-PHB cell mass (*e.g.*, alkaline treatment) or enzymatic digestion (protease based) can be combined with washing steps to obtain PHB-rich solids with reduced solvent consumption.[35] These green recovery options provide feasible pathways for translating the SCN–*C.N* biohybrid system toward sustainable PHB production.

4. Conclusions

This work demonstrates that semiconductor-induced photocatalysis and microbial metabolism function synergistically in a biohybrid system to drive PHB biosynthesis. Among the investigated semiconductors, SCN demonstrated better compatibility with *C.N*, enabling electron transfer enhancement, charge-transfer resistance reduction, and microbial viability improvement, thus collectively resulting in a marked PHB biosynthesizability. In addition, SCN also extended visible-light absorption, introduced carbon vacancies and enhanced interfacial charge separation, with these advantages rendering the effective coupling of its photochemical activity with microbial redox metabolism. Crucially, a central discovery was that the metabolic behaviors of *C.N* for photocatalytic PHB synthesis altered in the autotrophic and heterotrophic biohybrid systems. Specifically, the heterotrophic biohybrid system relied on carbon oxidation pathways involving glycolysis and the TCA cycle for heterotrophic PHB production, while the autotrophic biohybrid system utilized SCN-mediated photoelectron generation and CO_2 fixation through light-driven electron transport for autotrophic PHB production. This study elucidates SCN-mediated photoelectron transfer on reprogramming metabolic mechanisms in *C.N* for PHB synthesis, establishing a critical bridge between photonic energy conversion and biological redox processes. Our findings provide a novel framework for developing light-powered biohybrid systems for efficient carbon fixation and biopolymer synthesis.

Author contributions

Heng Li: writing – original draft, data curation, and conceptualization. Weidong Zhang: writing – original draft, investigation, and data curation. Ruixiang Zhao: methodology, investigation, and data curation. Haiyan Li: investigation and formal analysis. Dong Xia: writing – review & editing, and supervision. Yuanpeng Wang: writing – review & editing, supervision, and funding acquisition.

Conflicts of interest

There are no conflicts of interest to declare.

Data availability

The data that support the findings of this study are available from the corresponding author.

Supplementary information (SI) is available. See DOI: https://doi.org/10.1039/d5gc07072d.

Acknowledgements

This work was supported by the National Natural Science Foundation of China (U24A20543, 22038012) and the Science and Technology Program of Fujian Province, China (2025Y4001).

References

1 G. Chen and M. Patel, *Chem. Rev.*, 2012, **112**, 2082–2099.
2 S. Philip, T. Keshavarz and I. Roy, *J. Chem. Technol. Biotechnol.*, 2007, **82**, 233–247.
3 K. Sudesh, H. Abe and Y. Doi, *Prog. Polym. Sci.*, 2000, **25**, 1503–1555.
4 M. Koller, A. Salerno, M. Dias, A. Reiterer and G. Braunegg, *Food Technol. Biotechnol.*, 2010, **48**, 255–269.
5 L. Madison and G. Huisman, *Microbiol. Mol. Biol. Rev.*, 1999, **63**, 21–53.
6 J. Choi and S. Y. Lee, *Appl. Microbiol. Biotechnol.*, 1999, **51**, 13–21.
7 S. Y. Lee, *Biotechnol. Bioeng.*, 2015, **49**, 1–14.
8 K. Sakimoto, A. Wong and P. Yang, *Science*, 2016, **351**, 74–77.
9 C. Liu, J. Gallagher, K. Sakimoto, E. Nichols, C. Chang, M. Chang and P. Yang, *Nano Lett.*, 2015, **15**, 3634–3639.
10 Y. Zhang, X. Liu, Y. Zhang, Y. Zhang, W. Sun, W. Wang, X. Cao, X. Guo and C. Li, *J. Am. Chem. Soc.*, 2025, **147**, 25097–25106.
11 W. Yu, M. Pavliuk, A. Liu, Y. Zeng, S. Xia, Y. Huang, H. Bai, F. Lv, H. Tian and S. Wang, *ACS Appl. Mater. Interfaces*, 2023, **15**, 2183–2191.
12 B. Wang, Z. Jiang, J. Yu, J. Wang and P. Wong, *Nanoscale*, 2019, **11**, 9296–9301.
13 M. Xu, P. Tremblay, L. Jiang and T. Zhang, *Green Chem.*, 2019, **21**, 2392–2400.
14 J. Wang, M. Xu, P. Tremblay and T. Zhang, *Int. J. Biol. Macromol.*, 2022, **203**, 526–534.
15 M. Xu, P. Tremblay, R. Ding, J. Xiao, J. Wang, Y. Kang and T. Zhang, *Sci. Total Environ.*, 2021, **753**, 142050.
16 W. Dong, J. Cai, Q. Sun, L. Luan, X. Ji, S. Zeng and Y. Huang, *Green Chem. Eng.*, 2025, **6**, 518–537.
17 W. Wang, M. Zhang, M. Guo, J. Wang, X. Wang, J. Yin, L. Chen and Y. Li, *Green Chem.*, 2026, **28**, 213–224.
18 Y. Jiang, Y. Chai, Y. Jiang, S. Tian, Z. Wang, Y. Cao, C. H. Lam, J. J. Zhu, R. Lin and W. Zhu, *Chin. Chem. Lett.*, 2025, 111115.
19 S. Kumar, S. Karthikeyan and A. Lee, *Catalysts*, 2018, **8**, 74.

20 Y. Niu, J. Shen, W. Guo, X. Zhu, L. Guo, Y. Wang and F. Li, *Molecules*, 2023, **28**, 6412.
21 X. Fang, L. Ma, K. Liang, S. Zhao, Y. Jiang, C. Ling, T. Zhao, T. Cheang and A. Xu, *J. Mater. Chem. A*, 2019, **7**, 11506–11512.
22 J. Wu, Z. Xu, H. Sun, H. Rao, P. She and J. Qin, *Chem. Eng. J.*, 2025, **515**, 163381.
23 V. Dang, N. Nhung, I. Rabani, N. Tran, B. Thuy and H. Truong, *RSC Adv.*, 2025, **15**, 19088–19103.
24 L. Sharma and N. Mallick, *Bioresour. Technol.*, 2005, **96**, 1304–1310.
25 E. Gil-Fuster, J. Eisert and C. Bravo-Prieto, *Nat. Commun.*, 2024, **15**, 2277.
26 A. Mohammad, P. Chandra, M. Khan, C. Choi and T. Yoon, *Adv. Colloid Interface Sci.*, 2023, **322**, 103048.
27 Q. Lin, Z. Li, T. Lin, B. Li, X. Liao, H. Yu and C. Yu, *Chin. J. Chem. Eng.*, 2020, **28**, 2677–2688.
28 A. J. Bard and L. R. Faulkner, *Electrochemical Methods: Fundamentals and Applications*, Wiley, New York, 2nd edn, 2001.
29 F. Reinecke and A. Steinbüchel, *J. Mol. Microbiol. Biotechnol.*, 2009, **16**, 91–108.
30 J. Dong, Y. Zhang, M. Hussain, W. Zhou, Y. Chen and L. Wang, *Nanomaterials*, 2022, **12**, 121.
31 Y. Chen, W. Li, D. Jiang, K. Men, Z. Li, L. Li, S. Sun, J. Li, Z. Huang and L. Wang, *Sci. Bull.*, 2019, **64**, 44–53.
32 S. Morab, M. Sundaram and A. Pivrikas, *Coatings*, 2023, **13**, 1657.
33 X. Fang, S. Kalathil and E. Reisner, *Chem. Soc. Rev.*, 2020, **49**, 4926–4952.
34 J. Wang, J. Huang and S. Liu, *Biotechnol. Adv.*, 2024, **72**, 108340.
35 D. Nnabodo, E. O. Oke, M. Gackowski, J. Kryściak-Czerwenka, T. Miri, M. Keith, R. Karcz and M. Guzik, *Bioresour. Technol. Rep.*, 2025, **32**, 102323.